EVN observations of 6.7 GHz methanol maser polarization in massive star-forming regions. II. First statistical results

Surcis, G.; Vlemmings, W.H.T.; Langevelde, H.J. van; Hutawarakorn Kramer, B.; Quiroga-Nunez, L.H.

Astronomy & Astrophysics

EVN observations of 6.7 GHz methanol maser polarization in massive star-forming regions

II. First statistical results[*]

G. Surcis[1], W. H. T. Vlemmings[2], H. J. van Langevelde[1,3], B. Hutawarakorn Kramer[4,5], and L. H. Quiroga-Nuñez[6]

[1] Joint Institute for VLBI in Europe, Postbus 2, 7990 AA Dwingeloo, The Netherlands
  e-mail: surcis@jive.nl
[2] Chalmers University of Technology, Onsala Space Observatory, 439 92 Onsala, Sweden
[3] Sterrewacht Leiden, Leiden University, Postbus 9513, 2300 RA Leiden, The Netherlands
[4] Max-Planck Institut für Radioastronomie, Auf dem Hügel 69, 53121 Bonn, Germany
[5] National Astronomical Research Institute of Thailand, Ministry of Science and Technology, Rama VI Rd., 10400 Bangkok, Thailand
[6] Planetario de Bogotá, IDARTES, Calle 26 B No. 5 – 93, Bogotá, Colombia

ABSTRACT

Context. Magnetic fields have only recently been included in theoretical simulations of high-mass star formation. The simulations show that magnetic fields play an important role in the formation and dynamics of molecular outflows. Masers, in particular 6.7-GHz CH_3OH masers, are the best probes of the magnetic field morphologies around massive young stellar objects on the smallest scales of 10–100 AU.
Aims. Providing new observational measurements of the morphology of magnetic fields around massive young stellar objects by using 6.7-GHz CH_3OH maser emission is very important for setting constraints on the numerical simulations of massive star formation.
Methods. This paper focuses on 4 massive young stellar objects, IRAS 06058+2138-NIRS 1, IRAS 22272+6358A, S255-IR, and S231, which complement our previous 2012 sample (the first EVN group). From all these sources, molecular outflows have been detected in the past. Seven of the European VLBI Network antennas were used to measure the linear polarization and Zeeman-splitting of the 6.7-GHz CH_3OH masers in the star-forming regions in this second EVN group.
Results. We detected a total of 128 CH_3OH masing cloudlets. Fractional linear polarization (0.8%–11.3%) was detected towards 18% of the CH_3OH masers in our sample. The linear polarization vectors are well ordered in all the massive young stellar objects. We measured significant Zeeman-splitting in IRAS 06058+2138-NIRS 1 ($\Delta V_Z = 3.8 \pm 0.6$ m s^{-1}) and S255-IR ($\Delta V_Z = 3.2 \pm 0.7$ m s^{-1}).
Conclusions. By considering the 20 massive young stellar objects towards which the morphology of magnetic fields was determined by observing 6.7-GHz CH_3OH masers in both hemispheres, we find no evident correlation between the linear distributions of CH_3OH masers and the outflows or the linear polarization vectors. On the other hand, we present first statistical evidence that the magnetic field (on scales 10–100 AU) is primarily oriented along the large-scale outflow direction. Moreover, we empirically find that the linear polarization fraction of unsaturated CH_3OH masers is $P_l < 4.5\%$.

Key words. stars: formation – masers – polarization – magnetic fields

1. Introduction

Despite the likely importance of magnetic fields in the formation of low-mass stars (e.g., Matsumoto & Tomisaka 2004; McKee & Ostriker 2007), there are still only a few observations around massive young stellar objects (YSOs; e.g., Crutcher 2005; Vlemmings et al. 2006; Girart et al. 2009), and theoretical simulations of massive star formation have only recently included them (e.g., Banerjee & Pudritz 2007; Peters et al. 2011; Seifried et al. 2012a). Since massive stars are fully radiative, they are, with few exceptions (e.g., Donati et al. 2006; Alecian et al. 2012), not expected to have significant magnetic fields. Consequently, it has been thought that the magnetic fields do not play any role in their formation. However, the detection of molecular outflows in massive star-forming regions and their necessary inclusion in the main models (e.g., McKee & Tan 2003; Bonnell et al. 2004) makes the presence of magnetic fields

during the formation of high-mass stars unavoidable. These fields are very likely the magnetic field frozen into the collapsing protostellar envelope.

The formation of outflows has been observed in all simulations that include magnetic fields. Banerjee & Pudritz (2007) indicate that magnetic fields coupled to the prestellar disks could be the possible driving power for early outflows, which can be understood in terms of a growing magnetic tower. By producing cavities through which radiation pressure can be released, these early outflows reduce the limitations on the final mass of massive stars imposed by simply considering the gravitational collapse. The outflows seem to be relatively fast and well-collimated for low and intermediate magnetic intensities ($\mu^1 = 30–120$), and

---

[*] Appendix A is available in electronic form at
http://www.aanda.org

[1] To evaluate the importance of the magnetic fields it is fundamental to compare the mass to magnetic flux ratio (M/Φ) to the critical value of this ratio, $(M/\Phi)_{crit} \approx 0.12/\sqrt{G}$, that is $\mu = (M/\Phi)/(M/\Phi)_{crit}$. The stronger the magnetic field is, the lower μ is. If $\mu < 1$, the magnetic field can prevent the collapse (Mouschovias & Spitzer 1976).

more slowly and poorly collimated for stronger fields ($\mu \sim 5$; Hennebelle et al. 2011; Seifried et al. 2012a). Furthermore, Seifried et al. (2012a) show that magneto-centrifugally driven outflows consist of two regimes. In the first regime close to the disk and the rotation axis, acceleration is dominated by the centrifugal force; that is gas gets flung outwards along the poloidal magnetic field lines, whereas in the second regime farther away from the disk the toroidal magnetic field starts to dominate the acceleration. They also suggest that, for strong magnetic fields, the poorly collimated outflows are typical of the very early stage of massive star formation, and the collimation will subsequently increase because the launching of a well-collimated, fast jet overtakes the slowly expanding outflow. Peters et al. (2011) suggest two effects that tend to weaken and broaden the outflows. The first one comes from the disruption of the velocity coherence due to the gravitational fragmentation of the accretion flow. Second, the thermal pressure of ionized gas is higher than the magnetic pressure, so it is dynamically dominant within the H II region. Because the magnetically driven jets can survive until gravitational fragmentation disrupts uniform rotation, they therefore proposed the ionization feedback as a better driving source of the observed uncollimated outflows rather than the magnetic field.

Besides contributing to the formation of outflows, the simulations show that magnetic fields prevent fragmentation, reduce angular momentum via magnetic braking, and, marginally, influences the accretion rate (Banerjee & Pudritz 2007; Peters et al. 2011; Hennebelle et al. 2011; Seifried et al. 2011). The magnetic fields also play a significant role in the evolution of the circumstellar disk. While for weak magnetic fields, $\mu > 10$, Keplerian disks with sizes of a few 100 AU are easily formed, for strong magnetic fields ($\mu < 10$) the Keplerian disks are formed only if a turbulent velocity field is introduced in the simulations (Seifried et al. 2011, 2012b). Finally, magnetic fields determine also the size of H II regions that in the presence of strong magnetic field are generally smaller than without magnetic field (Peters et al. 2011).

Therefore, new measurements of the orientation and strength of magnetic fields at milliarcsecond (mas) resolution close to the massive YSOs are fundamental for providing new input for numerical simulations of massive star formation. Over the last years, the high importance of using masers as probes of magnetic fields on the smallest scales (10–100 AU) has been proven (e.g., Vlemmings et al. 2006, 2010; Surcis et al. 2011a, 2011b, 2012). In particular, the 6.7-GHz CH$_3$OH masers, which are among the most abundant maser species in massive star-forming regions, are playing a crucial role in determining the magnetic field morphology (e.g., Surcis et al. 2009, 2011b, 2012). Magnetic fields have mainly been detected along outflows and in a few cases on surfaces of disk/tori (Vlemmings et al. 2010; Surcis et al. 2009, 2011b, 2012). Moreover, 6.7-GHz CH$_3$OH masers are also ideal for measuring the Zeeman-splitting even though the exact proportionality between the measured splitting and the magnetic field strength is still uncertain (Vlemmings et al. 2011). Therefore, enlarging the number of massive YSOs towards which observations in full polarization of 6.7-GHz CH$_3$OH maser are made is of high importance. Here we show the results of our second EVN group composed of 4 massive star-forming regions, which are described in details in Sect. 2. The observations with the data reduction details are described in Sect. 3, while the codes used for our analysis are introduced in Sect. 4. The results, which are presented in Sect. 5, are discussed in Sect. 6, where we statistically analyze the sample composed of all the massive YSOs towards which the morphology

of magnetic fields was determined by observing the 6.7-GHz CH$_3$OH masers.

2. The second EVN group

We selected a subgroup of five massive star-forming regions among the northern hemisphere sources observed with the Effelsberg 100-m telescope (Vlemmings 2008; Vlemmings et al. 2011). Hereafter, we refer to this group as the second EVN group. Here, we present four of them while the results of IRAS 20126+4104 will be discussed in a subsequent paper along with the results from 22-GHz H$_2$O maser polarization observations. The sources were selected based on their high peak flux density to allow potential detection of Zeeman-splitting as well as the presence of molecular outflows.

2.1. IRAS 06058+2138-NIRS 1

IRAS 06058+2138 (better known as S252 or AFGL5180) is a near-infrared (NIR) cluster of YSOs at a parallax distance of 1.76 ± 0.11 kpc (Oh et al. 2010). Three massive clumps were identified in the region by Saito et al. (2007). The most massive one named MCS B coincides with the MM1 clump ($M \approx 50\ M_\odot$) detected at 1.2-mm by Minier et al. (2005). The massive YSO NIRS 1 ($V_{\rm lsr}^{\rm C^{18}O} = +3.9$ km s^{-1}, Saito et al. 2007; Tamura et al. 1991) is associated with MCS B and is also the 6.7-GHz CH$_3$OH maser site (Minier et al. 2000; Xu et al. 2009). The CH$_3$OH masers show a linear distribution of 120 mas with a roughly linear velocity gradient along it, although a few masers following a different velocity distribution (Minier et al. 2000). A CO-outflow (PA$_{\rm out}$ = 130°, Snell et al. 1988; Wu et al. 2010) is centered and perpendicular to the linear distribution of the CH$_3$OH masers (Wu et al. 2010). Wu et al. (2010) measured a velocity range for the blue-shifted and red-shifted lobes of -10 km s$^{-1} < V_{\rm IRAS\,06058}^{\rm blue} < -2$ km s^{-1} and $+8$ km s$^{-1} < V_{\rm IRAS\,06058}^{\rm red} < +20$ km s^{-1}, respectively. A Zeeman-splitting of the 6.7-GHz CH$_3$OH masers of $\Delta V_{\rm Z} = -0.49 \pm 0.15$ m s^{-1} was measured by Vlemmings et al. (2011) with the Effelsberg 100-m telescope.

2.2. IRAS 22272+6358A

IRAS 22272+6358A is a YSO deeply embedded in the bright-rimmed cloud L1206 (Sugitani et al. 1991). L1206 is located in the Local Arm at a parallax distance of $0.776^{+0.104}_{-0.083}$ kpc (Rygl et al. 2010). No radio continuum emission at 2 cm and 6 cm has been detected towards IRAS 22272+6358A (Wilking et al. 1989; McCutcheon et al. 1991) indicating that an H II region has not been formed yet. Considering also the low color temperature $T(60\ \mu m/100\ \mu m) \approx 38$ K measured by Casoli et al. (1986), IRAS 22272+6358A is a massive YSO at a very young phase (14.2 $M_\odot$ and $V_{\rm lsr} \simeq -11$ km s^{-1}; Beltrán et al. 2006). Beltrán et al. (2006) also observed a CO-outlow (PA$_{\rm out}$ = 140°) centered at the position of IRAS 22272+6358A with velocity ranges -19.5 km s$^{-1} < V_{\rm IRAS\,22272}^{\rm blue} < -13.5$ km s^{-1} and -8.5 km s$^{-1} < V_{\rm IRAS\,22272}^{\rm red} < -2.5$ km s^{-1} of the blue-shifted and red-shifted lobes, respectively.

At mas resolution two 6.7-GHz CH$_3$OH maser groups were detected, which are separated by $\sim$100 mas and associated with IRAS 22272+6358A. A third weak group of CH$_3$OH masers was also found northeast of the other two (Rygl et al. 2010). Vlemmings et al. (2011) measured a small Zeeman-splitting of the 6.7-GHz CH$_3$OH masers of $\Delta V_{\rm Z} = 0.53 \pm 0.15$ m s^{-1}.

Table 1. Observational details.

Source	Observation date	Pointing RA[a] (J2000) (^{h} : ^{m} : ^{s})	Pointing Dec[a] (J2000) ($^\circ$: $'$: $''$)	Calibrator	Beam size (mas × mas)	rms (mJy beam^{-1})
IRAS 06058+2138-NIRS1	May 30, 2011	06:08:53.344[b]	21:38:29.158[b]	J0927+3902	7.3 × 3.4	3
IRAS 22272+6358A	October 27, 2011	22:28:51.407[b]	64:13:41.314[b]	J2202+4216	6.7 × 4.3	4
S255-IR	October 30, 2011	06:12:54.020[b]	17:59:23.316[b]	J0359+5057	8.4 × 3.4	3
S231	October 27, 2011	05:39:13.059[c]	35:45:51.29[c]	J0359+5057	6.5 × 3.4	3

Notes. [a] The pointing position corresponds to the absolute position of the brightest maser spot measured from previous VLBI observations. [b] Position from Rygl et al. (2010). [c] Position from Minier et al. (2000).

2.3. S255-IR

S255-IR ($V_{lsr,CO}^{S255}$ = +5.2 km s^{-1}, Wang et al. 2011) is a famous star-forming region located between the two H II regions S255 and S257 at a parallax distance of $1.59^{+0.07}_{-0.06}$ kpc (Rygl et al. 2010). Minier et al. (2005) identified, with SCUBA, three mm sources in a dusty filament elongated north-south: MM1, MM2, and MM3. MM2, which contains three ultra-compact H II regions (UCH II), is associated with a NIR cluster of YSOs and appears to be the most evolved of the three regions (Minier et al. 2005). Wang et al. (2011) detected three 1.3 mm continuum peaks towards MM2 and the stronger one named as SMA 1 coincides with the near-infrared source NIRS 3 (Tamura et al. 1991), which drives an UCH II region (Wang et al. 2011).

6.7-GHz CH$_3$OH masers and 22-GHz H$_2$O masers are detected towards SMA 1 (Goddi et al. 2007; Wang et al. 2011). Because the H$_2$O masers are associated with the inner part of the jet/outflow system (PA$_{jet}$ = 67°, Howard et al. 1997; PA$_{out}^{CO}$ = 75°, Wang et al. 2011), NIR 3 is thought to be the driving source of this jet/outflow system and should not be older than 10^5 yr (Wang et al. 2011). The velocities of the blue-shifted and red-shifted lobes of the CO-outflow are −40 km s^{-1}< $V_{S255-IR}^{blue}$ < 0 km s^{-1} and +16 km s^{-1}< $V_{S255-IR}^{red}$ < +56 km s^{-1}, respectively (Wang et al. 2011). Wang et al. (2011) also detected a rotating toroid perpendicular to the outflow that fragmented into two sources SMA 1 and SMA 2.

A Zeeman-splitting of ΔV_Z = 0.47 ± 0.08 m s^{-1} for the 6.7-GHz CH$_3$OH masers was measured by Vlemmings et al. (2011).

2.4. S231

IRAS 05358+3543 is a cluster of embedded infrared sources associated with a number of H II regions ($V_{lsr}^{IRAS 05358}$ = −17.5 km s^{-1}, Ginsburg et al. 2009), among which S231, S233, and S235 (Israel & Felli 1978). Even if the 6.7-GHz CH$_3$OH maser site is surrounded by the three H II regions and it is not directly associated with any of them, the maser site is known in literature with the name S231 (e.g. Minier et al. 2000). Following Heyer et al. (1996), we adopt a kinematic distance of 1.8 kpc for the overall complex.

The CH$_3$OH masers show a linear distribution that was suggested to trace an edge-on disk (PA$_{CH_3OH}$ ≈ 25°, Minier et al. 2000), which is associated with one of the millimeter continuum sources identified by Beuther et al. (2007), i.e. mm1a. Beuther et al. (2007) suggested that mm1a, which is also associated with an hypercompact H II region and a mid-infrared source, forms a binary system with mm1b (with a projected

separation of 1700 AU). Ginsburg et al. (2009) observed mm1a with the VLA and they determined a projected separation between mm1a and the CH$_3$OH maser site of ~400 AU suggesting that probably the binary system is formed by mm1a and the massive YSO associated with the CH$_3$OH maser site. Furthermore, Ginsburg et al. (2009) associated one of the seven H$_2$-outflows detected towards this region, the collimated outflow 2 of which only the blue-shifted lobe is visible (PA$_{out}$ = 133° ± 5°, V_{S231}^{blue} ≈ −47 km s^{-1}), with the linear distribution of the CH$_3$OH masers. Vlemmings et al. (2011) measured a Zeeman-splitting of 0.95 ± 0.11 m s^{-1} of the CH$_3$OH masers.

3. Observations and data reduction

The sources were observed at 6.7-GHz in full polarization spectral mode with seven of the European VLBI Network[2] (EVN) antennas (Effelsberg, Jodrell, Onsala, Medicina, Torun, Westerbork, and Yebes-40 m), for a total observation time of 26 h (program code ES066). The bandwidth was 2 MHz, providing a velocity range of ~100 km s^{-1}. The data were correlated with the EVN software correlator (SFXC) at Joint Institute for VLBI in Europe (JIVE) using 2048 channels and generating all 4 polarization combinations (RR, LL, RL, LR) with a spectral resolution of ~1 kHz (~0.05 km s^{-1}). The observational details are reported in Table 1.

Because the observations were not performed in phase-referencing mode, we do not have information of the absolute positions of the masers. The pointing positions of our observations correspond to the absolute positions of the brightest maser spot of each source as measured from previous VLBI observations (see Table 1).

The data were edited and calibrated using AIPS. The bandpass, the delay, the phase, and the polarization calibration were performed on the calibrators listed in Table 1. Fringe-fitting and self-calibration were performed on the brightest maser feature of each star-forming region. The I, Q, U, and V cubes were imaged using the AIPS task IMAGR. The Q and U cubes were combined to produce cubes of polarized intensity ($P_l = \sqrt{Q^2 + U^2}$) and polarization angle ($\chi = 1/2 \times$ atan(U/Q)). We calibrated the linear polarization angles by comparing the linear polarization angles of the polarization calibrators measured by us with the angles obtained by calibrating the POLCAL observations made by NRAO[3]. IRAS 06058+2138 was observed a day after a POLCAL observations run and the polarization angle of
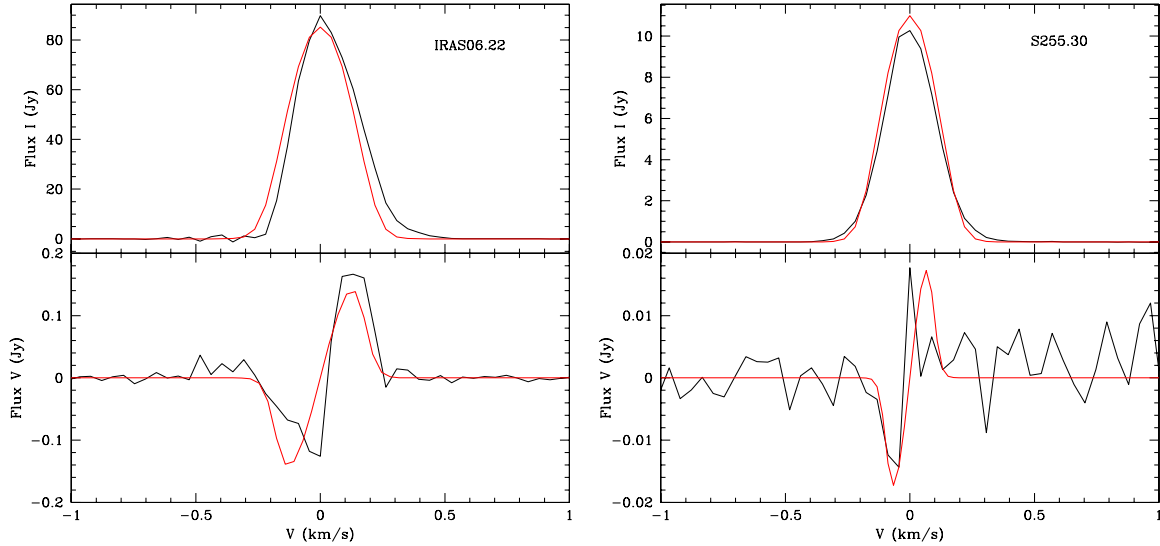
Fig. 1. Total intensity (*I, top*) and circular polarized (*V, bottom*) spectra for the two maser features IRAS 06.22 (*left panel*) and S255.30 (*right panel*), see Tables A.1 and A.3. The thick red lines are the best-fit models of *I* and *V* emission obtained using the adapted FRTM code (see Sect. 4). The maser features were centered to zero velocity.

J0927+3902 was $-85°2$. The other three sources were observed between two POLCAL observations runs during which the linear polarization angles were constant, the average values are $-74° \pm 4°$ and $-31° \pm 1°$ for J0359+5057 and J2202+4216, respectively. We were thus able to estimate the polarization angles with a systemic error of no more than ~5°. The formal errors on χ are due to thermal noise. This error is given by $\sigma_\chi = 0.5 \, \sigma_P/P \times 180°/\pi$ (Wardle & Kronberg 1974), where P and σ_P are the polarization intensity and corresponding rms error respectively.

4. Analysis

The CH$_3$OH maser features were identified by following the same procedure described in Surcis et al. (2011a). We made use of the adapted full radiative transfer method (FRTM) code for 6.7-GHz CH$_3$OH masers (Vlemmings et al. 2010; Surcis et al. 2011b; 2012) to model the total intensity and the linearly polarized spectrum of every maser feature for which we were able to detect linearly polarized emission.

The output of the code provides estimates of the emerging brightness temperature ($T_b\Delta\Omega$), i.e. the brightness temperature that emerges from the maser beam, and the intrinsic thermal linewidth (ΔV_i), i.e. the full width half-maximum (FWHM) of the Maxwellian distribution of particle velocities. Note that the shapes of the total intensity, linear polarization, and circular polarization spectra of the maser features depends on both $T_b\Delta\Omega$ and ΔV_i. Following Surcis et al. (2011b, 2012), we restricted our analysis to values of ΔV_i from 0.5 to 1.95 km s^{-1}. If $T_b\Delta\Omega > 2.6 \times 10^9$ K sr, the 6.7-GHz CH$_3$OH masers can be considered partially saturated and their ΔV_i and $T_b\Delta\Omega$ values are, respectively, overestimated and underestimated (Surcis et al. 2011b). However we can be confident that the orientation of their linear polarization vectors is not affected by their saturation state (Surcis et al. 2012), and consequently they can be taken into account for determining the orientation of the magnetic field in the region.

Considering $T_b\Delta\Omega$ and P_l we determined the angle between the maser propagation direction and the magnetic field (θ). If

$\theta > \theta_{crit} = 55°$, where θ_{crit} is the Van Vleck angle, the magnetic field appears to be perpendicular to the linear polarization vectors, otherwise it is parallel (Goldreich et al. 1973). To better determine the orientation of the magnetic field w.r.t. the linear polarization vectors we take into account the errors associated with θ, which we indicate here as ε^- and ε^+, i.e. $\theta^{\varepsilon^+}_{\varepsilon^-}$ in Tables A.1–A.4. We define the two limit values of the measured θ as $\theta^- = \theta - \varepsilon^-$ and $\theta^+ = \theta + \varepsilon^+$. Considering the critical value we have $\Delta^- = |\theta^- - 55°|$ and $\Delta^+ = |\theta^+ - 55°|$. If $\Delta^+ > \Delta^-$ the magnetic field is most likely perpendicular to the linear polarization vectors, if $\Delta^+ < \Delta^-$ the magnetic field is assumed to be parallel. Of course if θ^- and θ^+ are both larger or smaller than 55° the magnetic field is perpendicular or parallel to the linear polarization vectors, respectively.

Because of technical limitations, the spectral resolution of the past observations was of about 0.1 km s^{-1}, and we were only able to measure the Zeeman-splitting (ΔV_Z) from the cross-correlation between RR and LL spectra of the CH$_3$OH maser features (Surcis et al. 2009, 2011b, 2012). Nowadays, although using the same observing setup, the EVN SFXC at JIVE enables us to correlate the spectral data with a larger number of channels than previously possible on the JIVE hardware correlator (Schilizzi et al. 2001), providing a better spectral resolution (i.e., ~0.05 km s^{-1}). Because of this higher spectral resolution we can now determine the ΔV_Z by using the adapted FRTM code for 6.7-GHz CH$_3$OH maser, as was successfully done for H$_2$O masers by Surcis et al. (2011a). The best values for $T_b\Delta\Omega$ and ΔV_i are included in the code to produce the I and V models that were used for fitting the total intensity and circular polarized spectra of the CH$_3$OH masers (Fig. 1). The ΔV_Z measured in this way is physically more significant since the physical characteristics of the masers are taken into account.

5. Results

In Tables A.1–A.4 we list all the 128 CH$_3$OH maser features detected towards the 4 massive star-forming regions observed with the EVN. The description of the maser distribution and the polarization results are reported for each source separately in Sects. 5.1–5.4.
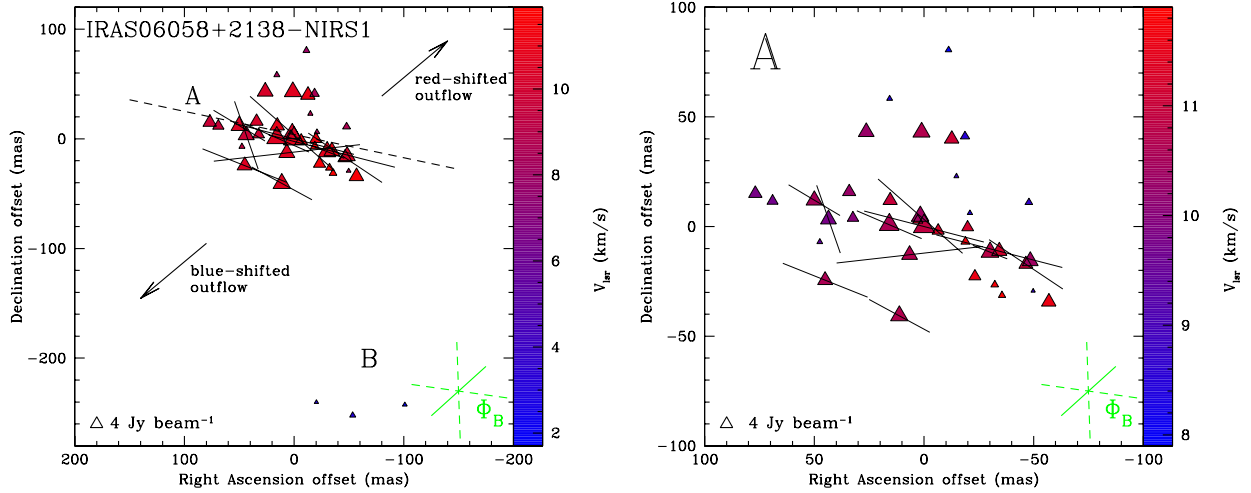
Fig. 2. *Left panel*: view of the CH$_3$OH maser features detected around IRAS 06058+2138-NIRS 1 (Table A.1). Triangles symbols identify CH$_3$OH maser features scaled logarithmically according to their peak flux density (Table A.1). Maser LSR radial velocities are indicated by color (the assumed velocity of the YSO is $V_{lsr}^{C^{18}O} = +3.9$ km s^{-1}, Saito et al. 2007). A 4 Jy beam^{-1} symbol is plotted for illustration. The linear polarization vectors, scaled logarithmically according to polarization fraction P_l, are overplotted. On the right-bottom corner the error weighted orientation of the magnetic field (Φ_B, see Sect. 6.2.1) is also reported, the two dashed segments indicates the uncertainty. The two arrows indicate the direction of the red- and blue-shifted lobe of the bipolar outflow (PA$_{out}$ = 130°; Wu et al. 2010). The dashed line is the best linear fit of the CH$_3$OH maser features of group A (PA$_{CH_3OH}$ = 78° ± 7°). *Right panel*: zoom-in view of group A.

5.1. IRAS 06058+2138-NIRS 1

We list all the identified 6.7-GHz CH$_3$OH maser features, which can be divided into two groups (A and B), in Table A.1, named as IRAS 06.01–IRAS 06.39. In the left panel of Fig. 2 we show all the 6.7-GHz CH$_3$OH maser features while in the right panel we show only the maser features of group A. The three maser features of group B were not detected in previous observations by Minier et al. (2000). Group A shows a linear distribution of about 140 mas (~250 AU) with a PA$_{CH_3OH}$ = 78° ± 7°, that is almost perpendicular to the direction of the CO-outflow (PA$_{out}$ = 130°, Wu et al. 2010). Although the velocity range of group A is similar to that reported by Minier et al. (2000), we do not see a clear linear velocity gradient, indicating that the masers are not likely tracing an edge-on Keplerian disk, but they trace more complex dynamics. The velocities of group A, which are red-shifted w.r.t. the velocity of NIRS 1, fall within the velocity range of the red-shifted lobe of the CO-outflow and they may be related to its structure. Instead the velocities of group B are slightly blue-shifted w.r.t. the velocity of NIRS 1 but do not fall within the velocity range of the blue-shifted lobe.

We detected linear polarization in 11 CH$_3$OH maser features ($P_l = 1.3\%-9.2\%$), all of which exclusively belong to group A. The adapted FRTM code was able to properly fit almost half of them. The results of the code are reported in Cols. 10, 11, and 14 of Table A.1. Three of the maser features are partially saturated, i.e. IRAS 06.09, IRAS 06.22, and IRAS 06.30. Although all the θ angles (Col. 14) are greater than $\theta_{crit} = 55°$, Δ^+ is smaller than Δ^- for IRAS 06.30 indicating that in this case the magnetic field is more likely parallel to the linear polarization vector. We measured a Zeeman-splitting of $\Delta V_Z = 3.8 \pm 0.6$ m s^{-1} for the brightest maser feature IRAS 06.22, its circular polarization fraction is $P_V = 0.3\%$.

5.2. IRAS 22272+6358A

We detected 26 6.7-GHz CH$_3$OH maser features towards IRAS 22272+6358A (Fig. 3), which are named
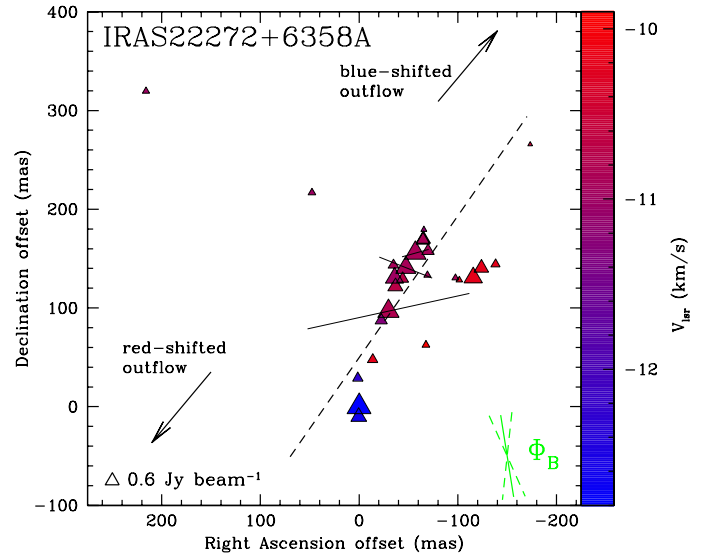
Fig. 3. View of the CH$_3$OH maser features detected around IRAS 22272+6358A (Table A.2). Same symbols as in Fig. 2. The assumed velocity of the YSO is $V_{lsr} = -11$ km s^{-1} (Beltrán et al. 2006). The two arrows indicate the direction of the red- and blue-shifted lobe of the bipolar outflow (PA$_{out}$ = 140°; Beltrán et al. 2006). The dashed line is the best linear fit of the CH$_3$OH maser features (PA$_{CH_3OH}$ = 145° ± 11°).

IRAS 22.01–IRAS 22.26 in Table A.2. The maser features show a linear distribution of 326 mas (~250 AU), with a position angle of PA$_{CH_3OH}$ = 145° ± 11°, that seems aligned with the CO-outflow (PA$_{out}$ = 140°; Beltrán et al. 2006). Two maser features, IRAS 22.25 and IRAS 22.26, are detected at a distance of about 130 mas (~100 AU) and 330 mas (~250 AU) from the linear distribution. One of them was also detected by Rygl et al. (2010). The line-of-sight velocity of the CH$_3$OH maser
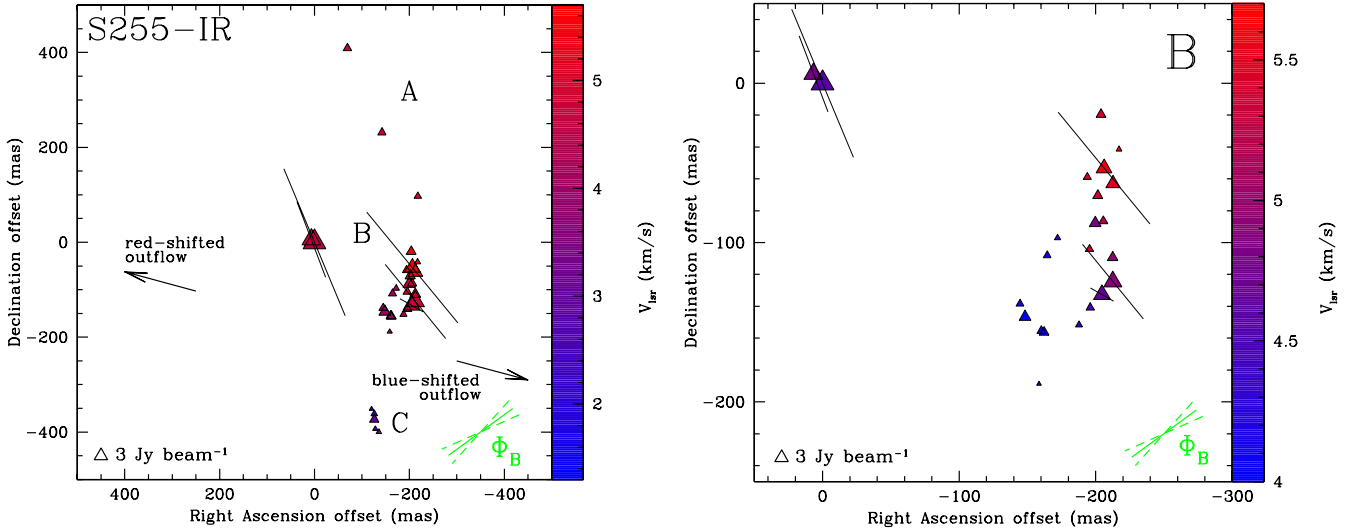
Fig. 4. *Left panel*: view of the CH$_3$OH maser features detected around S255-IR (Table A.3). *Right panel*: zoom-in view of group B. Same symbols as in Fig. 2. The assumed velocity of the YSO is $V_{lsr} = +5.2$ km s^{-1} (Wang et al. 2011). The two arrows indicate the direction of the red- and blue-shifted lobe of the bipolar outflow (PA$_{out}$ = 75°; Wang et al. 2011).

emission occurs within 2 km s^{-1} from the systemic velocity of the region.

Linearly polarized emission was detected towards 3 CH$_3$OH maser features ($P_l = 0.8\%-1.7\%$), which were all successfully modeled by the adapted FRTM code. They all appear unsaturated. The θ angles are greater than 55° indicating that the magnetic field is perpendicular to the linear polarization vectors. The rms noise of our observations did not allowed us to detect circular polarization at 5σ for any of the maser features ($P_V < 0.4\%$).

5.3. S255-IR

In the left panel of Fig. 4 all the 31 CH$_3$OH maser features are shown, which are listed in Table A.3 (named as S255.01–S255.31). The CH$_3$OH maser features can be divided in three groups (A, B, and C) based on the overall spatial distribution and similar line-of-sight velocities. While groups B and C were also detected previously (e.g., Goddi et al. 2007) the maser features of group A were undetected. The overall spatial distribution of the maser emission is mainly extended on an arch structure along the N-S direction, perpendicular to the CO-outflow (PA$_{out}$ = 75°, Wang et al. 2011), with the most blue-shifted masers w.r.t. the systemic velocity of S255-IR clustered to the south.

A linear polarization fraction between 1% and 4.5% was measured for 5 CH$_3$OH maser features. The adapted FRTM code indicates that only the brightest feature S255.30 is partially saturated because it measures $T_b\Delta\Omega = 3.2 \times 10^9$ K. For all the maser features $\theta > 55°$, so also in this case the magnetic field is perpendicular to the linear polarization vectors. A 6.7-GHz CH$_3$OH maser Zeeman-splitting of $\Delta V_Z = 3.2 \pm 0.7$ m s^{-1} was measured for S255.30.

5.4. S231

32 CH$_3$OH maser features were detected towards S231. They are named in Table A.4 as S231.01–S231.32 and are shown in Fig. 5. Following the naming convention adopted by Minier et al. (2000), the maser features are divided in four groups (A, B, C,

and D). Actually, group D was not detected by Minier et al. (2000). Furthermore, we have divided group A in two subgroups (A$_1$ and A$_2$) the second of which was also undetected by Minier et al. (2000). The overall maser emission is distributed along two preferential directions. One is outlined by group A and it is almost perpendicular to the direction of the bipolar outflow with a position angle of PA$_{CH_3OH}^A$ = 28° ± 8°, which is consistent with what was measured by Minier et al. (2000), and with a size of about 140 mas (~250 AU). A second direction is identified by combining groups B, C, and D and has an orientation (PA$_{CH_3OH}^{BCD}$ = 147° ± 12°) in agreement within the errors with the position angle of the outflow (PA$_{out}$ = 133° ± 5°, Ginsburg et al. 2009).

Because we cannot associate the maser emission with an individual YSO unambiguously, we compare the maser velocities with the average velocity of the parent molecular cloud ($V_{lsr}^{IRAS\,05358} = -17.5$ km s^{-1}). All the velocities of the maser features are red-shifted w.r.t. $V_{lsr}^{IRAS\,05358}$ by more than 2 km s^{-1}.

We measured linear polarized emission from CH$_3$OH maser features of group A and C, with a polarization fraction 0.8% < P_l < 11.3%, with the lowest one from group C. From the $T_b\Delta\Omega$ values obtained using the adapted FRTM code we found that three maser features out of five are partially saturated, all of which are part of group A. In S231 the magnetic field is also perpendicular to the linear polarization vectors. No 6.7-GHz CH$_3$OH maser Zeeman-splitting was measured in this source, unlike IRAS 22272+6358A, pointing to a relatively weak magnetic field ($P_V < 0.06\%$).

6. Discussion

6.1. The linear polarization fraction and the saturation state of CH$_3$OH masers

Modeling the total and the linearly polarized intensity of CH$_3$OH masers with the adapted FRTM code enables us not only to derive the orientation of the magnetic fields and to measure the Zeeman-splittings accurately, but also to estimate the saturation state of the CH$_3$OH masers.
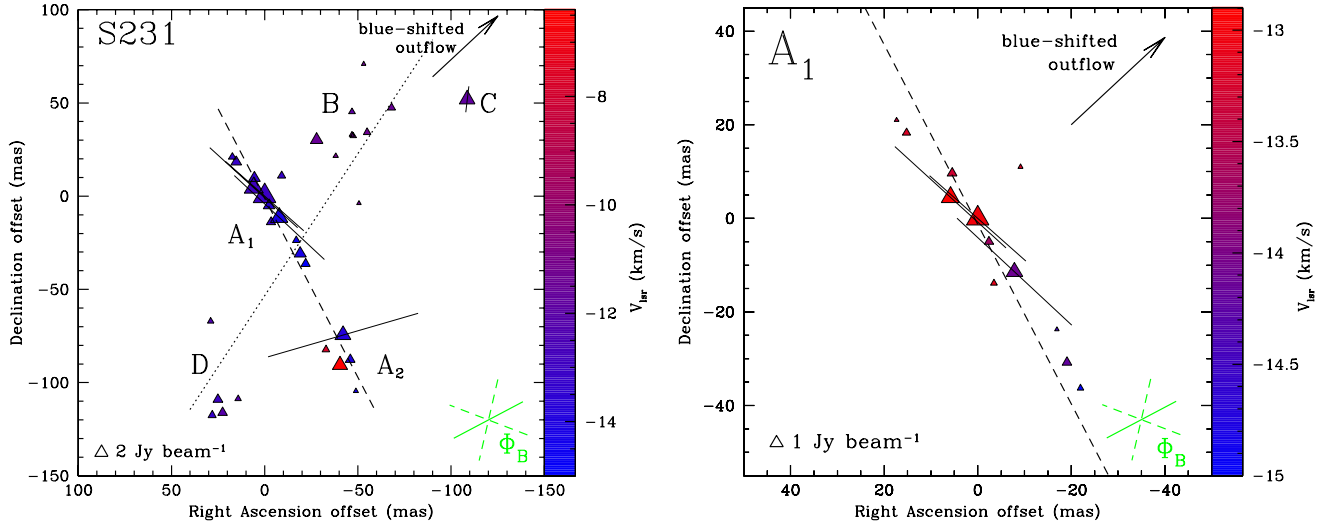
Fig. 5. *Left panel*: view of the CH$_3$OH maser features detected around S231 (Table A.4). *Right panel*: zoom-in view of group A1. Same symbols as in Fig. 2. The arrow indicates the direction of the blue-shifted lobe of the H_2-outflow (PA$_{out}$ = 133°; Ginsburg et al. 2009).The dashed line is the best linear fit of the CH$_3$OH maser features of group A (PA$^A_{CH_3OH}$ = 28° ± 8°), while the dotted line is the best linear fit of the CH$_3$OH maser features of groups B, C, and D (PA$^{BCD}_{CH_3OH}$ = 147° ± 12°).

As we have already mentioned in Sect. 4, the 6.7-GHz CH$_3$OH maser can be considered partially saturated if $T_b\Delta\Omega >$ 2.6×10^9 K sr. Surcis et al. (2011b) derived this value by considering the stimulated emission rate (R) and the theoretical condition for masers unsaturated or saturated. We refer the reader to Surcis et al. (2011b) for more details. The information of the unsaturated or saturated state of the maser was used by Surcis et al. (2012) to determine a correlation between the saturation state of the CH$_3$OH masers and their linear polarization fraction (P_l). They found that the 6.7-GHz CH$_3$OH masers with $P_l \lesssim 4.5\%$ are unsaturated. Adding the 19 new CH$_3$OH masers that we have detected in this work, for which it has been possible to determine $T_b\Delta\Omega$, to the previous measured 72 masers we confirm the value of 4.5% as found by Surcis et al. (2012) but with the exception of IRAS 06.30 (see Fig. 6 and Table 2). The model of IRAS 06.30 is probably influenced by the brightest maser (IRAS 06.22), which is located within 15 mas. This maser is twice a bright and highly linearly polarized.

6.2. Magnetic fields in the second EVN group

6.2.1. Magnetic field orientations

Before discussing the orientation of magnetic fields in the four massive YSOs, it is important to estimate whether the medium between the source and the observer could produce a significant rotation of the linear polarization vectors. This phenomenon is known as foreground Faraday rotation (Φ_f) and, as derived for the 6.7-GHz CH$_3$OH maser by Surcis et al. (2012), it can be written as

$$\Phi_f[°] = 2.26 \left(\frac{D}{[kpc]} \right), \tag{1}$$

where they assumed for the homogeneous interstellar electron density $n_e \approx 0.012$ cm^{-3} and for the interstellar magnetic fields $B_\parallel \approx 2$ μG. Because the massive star-forming regions investigated so far are at a distance of a few kpc, Φ_f is estimated to be within the errors of the linear polarization angles of the CH$_3$OH maser emission (Surcis et al. 2009, 2011b, 2012). This
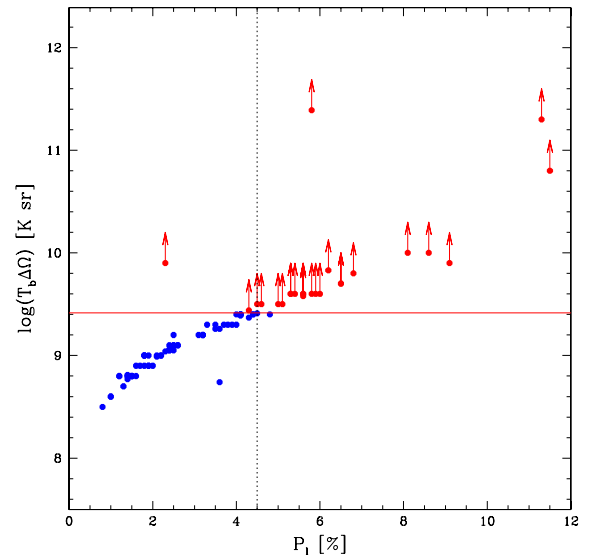
Fig. 6. Emerging brightness temperatures ($T_b\Delta\Omega$) as function of the linear polarization fraction (P_l). The blue and red circles indicate the unsaturated and saturated masers, respectively, detected in NGC 7538 (Surcis et al. 2011a), W51, W48, IRAS 18556+0138, and W3(OH) (Surcis et al. 2012), IRAS 06058+2138-NIRS1, IRAS 22272+6358A, S255-IR, and S231 (this work). The red arrows indicate that the $T_b\Delta\Omega$ values obtained from the adapted FRTM code are lower limits. The red full line is the limit of emerging brightness temperature above which the CH$_3$OH masers are considered saturated ($T_b\Delta\Omega >$ 2.6×10^9 K sr; Surcis et al. 2011a), and the dotted line gives the lower limit to the linear polarization fraction for saturated masers ($P_l \approx 4.5\%$, Surcis et al. 2012).

is also true in the case of the four YSOs presented in this work, for which Φ_f is estimated to range between about 2° and 4°.

Another effect that may affect the measurements of the linear polarization vectors is the internal Faraday rotation. Surcis et al. (2012) argued that because the linear polarization vectors of 6.7-GHz CH$_3$OH masers are quite accurately aligned

Table 2. Comparison between position angle of magnetic field, CH₃OH maser distribution, outflows, and linear polarization angles.

Source	$\langle\chi\rangle$ (°)	$\langle\Phi_B\rangle$ (°)	PA$_{out}$ (°)	PA$_{CH_3OH}$ (°)	ρ	$|PA_{out} - \langle\Phi_B\rangle|$ (°)	$|PA_{CH_3OH} - \langle\chi\rangle|$ (°)	$|PA_{CH_3OH} - PA_{out}|$ (°)	Ref.
Cepheus A	−57 ± 28	+30 ± 19^a	+40 ± 4^b	−79 ± 9	−0.34	10 ± 19	22 ± 29	61 ± 10^c	(1), (2)
W75N-group A	−13 ± 9	+77 ± 9^a	+66 ± 15^d	+43 ± 10	+0.96	11 ± 18	56 ± 14	23 ± 18	(3), (4)
NGC 7538-IRS1	−30 ± 69	+67 ± 70^a	−40 ± 10^e	+84 ± 7^f	+0.15	73 ± 71^c	66 ± 69^c	56 ± 12^c	(5), (6), (7)
W3(OH)-group II	+21 ± 45	−47 ± 44^a	–	−59 ± 6	−0.84	–	80 ± 45	–	(8)
W51-e2	+33 ± 16	−60 ± 21^a	−50 ± 20^g	+57 ± 8	+0.70	10 ± 29	24 ± 18	73 ± 22^c	(8), (9), (10)
IRAS 18556+0138	−2 ± 11	+88 ± 11^a	+58 ± 23^h	−40 ± 2	−0.99	30 ± 26	42 ± 11	82 ± 23^c	(8), (11)
W48	+23 ± 7	−67 ± 7^a	–	+55 ± 10	+0.70	–	78 ± 12	–	(8)
IRAS 06058+2138-NIRS1	+49 ± 47	−49 ± 52^a	−50 ± 15^i	+78 ± 7	+0.64	1 ± 54	29 ± 48	52 ± 17^c	(12), (13)
IRAS 22272+6358A	−80 ± 15	+9 ± 15^a	−40 ± 15^d	−35 ± 11	−0.87	49 ± 21	45 ± 19	5 ± 19	(12), (14)
S255-IR	+36 ± 12	−54 ± 12^a	+75 ± 15^d	−63 ± 49^j	−0.11	51 ± 19^c	81 ± 51^c	42 ± 51^c	(12), (15)
S231	+28 ± 49	−62 ± 49^a	−47 ± 5	+28 ± 8	+0.97	15 ± 49	0 ± 50	75 ± 9	(12), (16)
G291.27-0.70	−32 ± 5	+52 ± 5	–	−77 ± 14^k	–	–	45 ± 15	–	(17)
G305.21+0.21	−51 ± 14	28 ± 14	–	+48 ± 23^l	–	–	81 ± 27^c	–	(17), (18)
G309.92+0.47	+2 ± 56	−75 ± 56	–	+35 ± 5^l	–	–	33 ± 56	–	(17), (18)
G316.64-0.08	−67 ± 36	+21 ± 36	–	+34 ± 29^l	–	–	79 ± 46^c	–	(17)
G335.79+0.17	+44 ± 28	−41 ± 28	–	−69 ± 25^l	–	–	67 ± 38^c	–	(17), (18)
G339.88-1.26	+77 ± 24	−12 ± 24	–	−60 ± 17^l	–	–	43 ± 29^c	–	(17), (18)
G345.01+1.79	+5 ± 39	−86 ± 39	–	+74 ± 4^l	–	–	69 ± 39	–	(17), (18)
NGC 6334F (central)	+77 ± 20	−13 ± 20	–	−41 ± 16^k	–	–	62 ± 26^c	–	(17)
NGC 6334F (NW)	−71 ± 20	+19 ± 20	–	−80 ± 38^k	–	–	9 ± 43	–	(17)

Notes. $^{(a)}$ Before averaging we use the criterion described in Sect. 4 to estimate the orientation of the magnetic field w.r.t. the linear polarization vectors. $^{(b)}$ It has been obtained by flux weighting the angles reported in Table 2 of Curiel et al. (2006). $^{(c)}$ The differences between the angles are evaluated taking into account that PA ≡ PA ± 180°, $\langle\chi\rangle ≡ \langle\chi\rangle$ ± 180°, and $\langle\Phi_B\rangle ≡ \langle\Phi_B\rangle$ ± 180°. $^{(d)}$ We consider an arbitrary conservative error of 15°. $^{(e)}$ The errors are evaluated considering the minimum and maximum PA of the CO-outflows reported by Scoville et al. (1986). $^{(f)}$ We do not consider group E of CH₃OH masers in the fit. $^{(g)}$ Keto & Klaassen (2008) reported that the orientation of the outflow is along the rotation axis of the molecular accretion flows. So we evaluate the arithmetic mean value (PA$_{out}$) of the rotation axes measured from the CH₃CN (PA$_{CH_3CN}$ = 110°; Zhang et al. 1998) and the H53α flows (PA$_{H53\alpha}$ = 150°; Keto & Klaassen 2008). $^{(h)}$ We overestimate the errors by considering half of the opening angle of the outflow. $^{(i)}$ The PA$_{out}$ has been estimated from Fig. 4 of Wu et al. (2010). $^{(j)}$ S255.30 and S255.31 were not included in the fit. $^{(k)}$ The errors are overestimated by considering Figs. 1, 5, 9, and 10 of Dodson & Moriarty (2012). $^{(l)}$ The errors are equal to the difference between the angles determined by Dodson & Moriarty (2012) and by De Buizer (2003).

References. (1) Vlemmings et al. (2010); (2) Curiel et al. (2006); (3) Surcis et al. (2009); (4) Hunter et al. (1994); (5) Surcis et al. (2011b); (6) Scoville et al. (1986); (7) Kameya et al. (1989); (8) Surcis et al. (2012); (9) Keto & Klaassen (2008); (10) Zhang et al. (1998); (11) Gibb et al. (2003); (12) This work; (13) Wu et al. (2010); (14) Beltrán et al. (2006); (15) Wang et al. (2011); (16) Ginsburg et al. (2009); (17) Dodson & Moriarty (2012); (18) De Buizer (2003).

in each source, the internal Faraday rotation should be negligible. This general result applies also to the sources presented here. Furthermore, the saturation state of the masers seems to not affect the linearly polarized emission of CH₃OH masers as also noted by Surcis et al. (2012).

In the following, we discuss separately the orientation of the magnetic field in each of the current sources.

IRAS 06058+2138-NIRS1. We measured θ angles for six out of 11 CH₃OH masers. For the CH₃OH masers for which we could not measure the θ angles we supposed that $\theta > 55°$, as generally found (Surcis et al. 2011b, 2012). Moreover, we measured $\Delta^+ < \Delta^-$ only for the CH₃OH maser IRAS 06.30, which means that the magnetic field is parallel to its linear polarization vector (see Sect. 4). As a result, the error weighted orientation of the magnetic field is $\langle\Phi_B\rangle = 131° \pm 52°$ indicating that the magnetic field is along the bipolar CO-outflow (PA$_{out}$ = 130°; Wu et al. 2010). Remembering that if $\Delta V_Z > 0$ the magnetic field is pointing away from the observer and if $\Delta V_Z < 0$ towards the observer, from the Zeeman-splitting measurements we can also state that the magnetic field is pointing away from us.

IRAS 22272+6358A. The magnetic field is perpendicular to all the linear polarization vectors measured towards the source, i.e. $\langle\Phi_B\rangle = 9° \pm 15°$. The orientation of the magnetic field is rotated

by about 50°, i.e. within 3σ, w.r.t. the direction of both the CO-outflow and the linear distribution of the CH₃OH masers. The magnetic field might be along the extended north-south component of the C^{18}O emission detected by Beltrán et al. (2006). By looking at each single linear polarization vectors (Fig. 3), we speculate that the CH₃OH masers might probe a twisted magnetic field around the linear distribution of masers, or around the CO-outflow.

S255-IR. According to the linear polarization vectors and to the measured θ angles, the magnetic field has an error weighted orientation of $\langle\Phi_B\rangle = 126° \pm 12°$. In this case the magnetic field is not aligned with the CO-outflow (PA$_{out}$ = 75°; Wang et al. 2011) but it may be associated with the rotating torus (PA$_{torus}$ = 165°; Wang et al. 2011), like what was measured in NGC 7538-IRS1 (Surcis et al. 2011b). Also in this case, according to ΔV_Z, the magnetic field is pointing away from us. Since the spatial distribution of the H₂O masers in S255-IR is well aligned with the outflow direction (Goddi et al. 2007), interferometric polarization observations of H₂O masers will be crucial for interpreting the overall magnetic field morphology.

S231. The error-weighted orientation of the magnetic field is $\langle\Phi_B\rangle = 118° \pm 49°$. Despite that the angle of the linear polarization vector of S231.11 is more than one hundred degrees

misaligned with the other vectors, the magnetic field is along both to the CO-outflow (PA$_{out}$ = 133° ± 5°; Ginsburg et al. 2009) and to the linear fit of groups B, C, and D (PA$_{CH_3OH}^{BCD}$ = 147° ±12°; see Sect. 5.4).

6.3. The importance of magnetic fields in high-mass star formation

The importance of magnetic field in star-forming regions can be estimated by evaluating the ratio β between thermal and magnetic energies. If $\beta < 1$ the magnetic field is dynamically important. To measure β we need to know the magnetic field strength. As we mentioned in Sect. 1 the Landé g-factor of the 6.7-GHz CH$_3$OH transition, from which α_Z is evaluated, is still uncertain (Vlemmings et al. 2011). Consequently we can only parametrize the ratio β as function of α_Z by considering the Eq. (2) of Surcis et al. (2012)

$$\beta = 611.6 \, \alpha_Z^2 \cos\langle\theta\rangle \left(\frac{|\Delta V_Z|}{[\mathrm{m\,s^{-1}}]}\right)^{-2}. \qquad (2)$$

We find that $\beta_{\mathrm{IRAS\,06.22}} \simeq 12.4 \times \alpha_Z^2$ and $\beta_{\mathrm{S255.30}} \simeq 8 \times \alpha_Z^2$. Considering a reasonable value for α_Z in the range 0.005 km s^{-1} G^{-1} < α_Z < 0.05 km s^{-1} G^{-1} (Surcis et al. 2011b), we have a range of β between 10^{-4} and 10^{-2} for both sources. As it was found for all the previous massive star-forming regions investigated using the 6.7-GHz CH$_3$OH maser emission (Surcis et al. 2009, 2011b, 2012), magnetic fields play an important role in the dynamics of IRAS 06058+2138-NIRS1 and S255-IR.

6.4. Magnetic fields and outflows

In the last four years a total of 20 massive star-forming regions were observed at mas resolution at 6.7-GHz all over the sky to measure the orientation of magnetic fields around massive YSOs. They all are listed in Table 2. In the northern hemisphere the sources were observed using the EVN (Surcis et al. 2009, 2011b, 2012, and this work) and the Multi-Element Radio Linked Interferometer network (MERLIN) (Vlemmings et al. 2010), while in the southern hemisphere by using the Australia Telescope Compact Array (ATCA) (Dodson & Moriarty 2012). This total sample, which we refer to as the magnetic field total sample, gives us the opportunity to start a statistical analysis of the results so far.

We compare the orientation of the CH$_3$OH maser distribution (PA$_{CH_3OH}$, Col. 5 of Table 2) with the error weighted value of the linear polarization angles ($\langle\chi\rangle$, Col. 2) and with the orientation of the molecular outflows (PA$_{out}$, Col. 4), i.e. |PA$_{CH_3OH}$ − $\langle\chi\rangle$| (Col. 8) and |PA$_{CH_3OH}$ − PA$_{out}$| (Col. 9) respectively. In Col. 6 the correlation coefficients (ρ) of the linear fits made by us are also reported. For our statistical analysis we require the uncertainties of all the angles. While the errors of PA$_{CH_3OH}$ and $\langle\chi\rangle$ are easily determined, the uncertainties of PA$_{out}$ are unknown for most of the sources, so either, when possible, we estimate them (see footnotes of Table 2) or we consider a conservative uncertainty of ±15°. Moreover, we also compare the error weighted orientation of the magnetic field ($\langle\Phi_B\rangle$, Col. 3) with PA$_{out}$, i.e. |PA$_{out}$ − $\langle\Phi_B\rangle$| in Col. 7, for the 9 sources for which an outflow has been detected. Note that all the angles in Table 2 are the projection on the plane of the sky. The uncertainties in Cols. 7–9 are equal to $\sigma_{x-y} = \sqrt{\sigma_x^2 + \sigma_y^2}$, where x and y are the two angles taken in consideration in each column.

Table 3. Results of Komogorov-Smirnov test.

Angle	N	D	λ	$Q_{K-S}(\lambda)$
|PA$_{CH_3OH}$ − $\langle\chi\rangle$|	20	0.17	0.78	0.60
|PA$_{CH_3OH}$ − PA$_{out}$|	9	0.24	0.76	0.60
|PA$_{out}$ − $\langle\Phi_B\rangle$|	9	0.39	1.23	0.10

Figure 7 shows the probability distribution function (PDF) and the cumulative distribution function (CDF) of the projected angles |PA$_{CH_3OH}$ − $\langle\chi\rangle$| and |PA$_{CH_3OH}$ − PA$_{out}$|. Because the angles for the different sources have different errors, which need to be taken into account, we treat in Fig. 7 the full distributions instead of the histograms. The CDFs show that there is currently no indication of a relation between PA$_{CH_3OH}$ and the angles $\langle\chi\rangle$ and PA$_{out}$. Indeed, a Kolmogorov-Smirnov (K-S) test shows that the probabilities that |PA$_{CH_3OH}$ − $\langle\chi\rangle$| and |PA$_{CH_3OH}$ − PA$_{out}$| are drawn from random distributions (dashed lines in Fig. 7), i.e. all angular differences are equally likely, are in both cases ~60%. In Table 3 the results of the K-S test are reported, where D (Col. 3) is the maximum value of the absolute difference between the data set, composed of N (Col. 2) elements, and the random distribution, and

$$Q_{K-S}(\lambda) = 2 \sum_{j=1}^{N} (-1)^{j-1} e^{-2j^2\lambda^2} \qquad (3)$$

in Col. 5 is the significance level of the test. Here $\lambda = (\sqrt{N} + 0.12 + 0.11/\sqrt{N}) \times D$ (Col. 4). The K-S test becomes asymptotically accurate as N becomes large.

On the contrary, if we consider the angle between PA$_{out}$ and $\langle\Phi_B\rangle$ we find that the outflows are primarily oriented along the magnetic fields. The corresponding CDF is shown in Fig. 8 where, as in Fig. 7 we treat the full distributions, the dashed line is the CDF of a random distribution of the angles. The K-S test in this case gives a probability of about 10%.

Although the sample is still small, this statistical analysis suggests that the magnetic fields close to the central YSO (<1000 AU) are likely correlated with the direction of the large-scale outflows (~1 pc) detected in massive star-forming regions. At the same time any biases introduced in the magnetic field angles due to for example compression of maser gas are ruled out. To improve the statistics it is important to enlarge the number of sources of the magnetic field total sample for which the orientation of the molecular outflow is well determined. To do this, we are carrying out a large campaign to observe outflow tracers towards several massive star-forming regions.

7. Conclusions

We observed 4 massive star-forming regions at 6.7-GHz in full polarization spectral mode with the EVN to detect the linearly and circularly polarized emission of CH$_3$OH masers. We detected a total of 128 6.7-GHz CH$_3$OH masers and linearly polarized emission towards 24 of them. The linear polarization fraction is between 0.8% and 11.3%. We were also able to measure Zeeman-splitting in IRAS 06058+2138-NIRS 1 (ΔV_Z = 3.8 ± 0.6 m s^{-1}) and S255-IR (ΔV_Z = 3.2 ± 0.7 m s^{-1}).

We considered all the massive star-forming regions observed in full polarization mode at 6.7-GHz, so far, anywhere on the sky. By comparing the projected angles between magnetic fields and outflows, we find evidence that the magnetic field around massive YSOs are primarily oriented along the
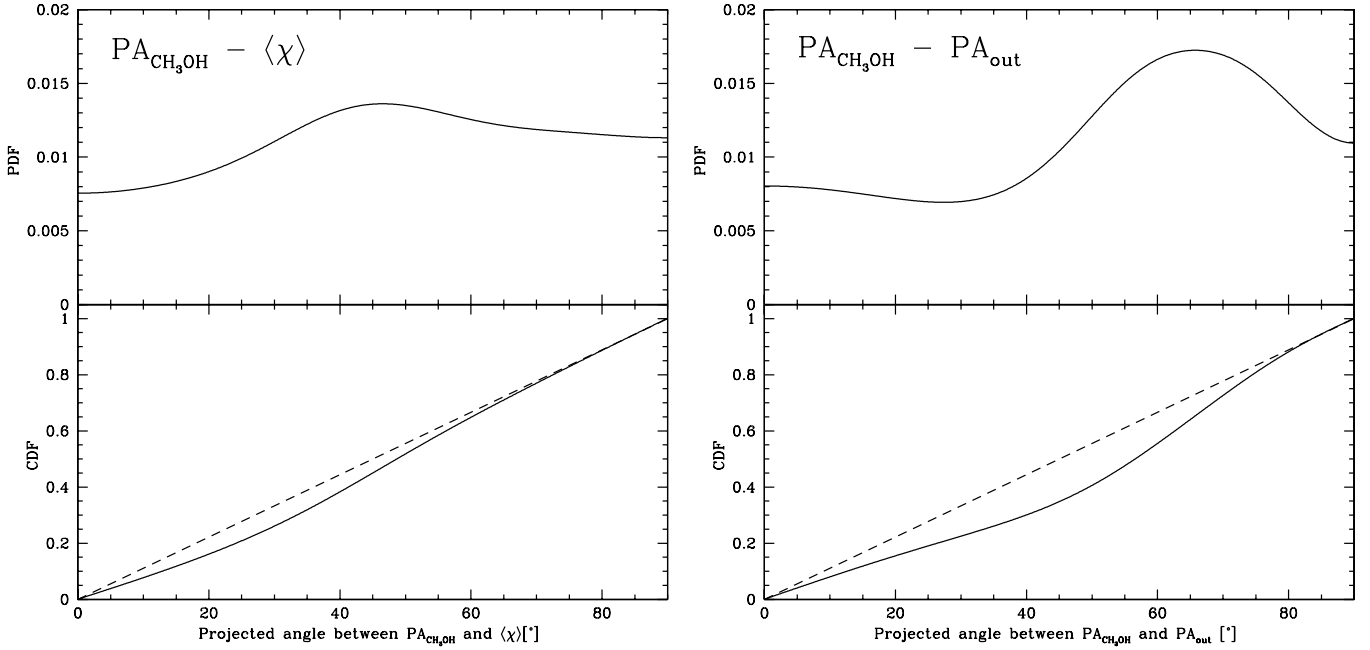
Fig. 7. *Left*: probability distribution function (PDF, *top panel*) and cumulative distribution function (CDF, *bottom panel*) of the projected angle between the PA of the CH$_3$OH maser distribution and the linear polarization angles ($|PA_{CH_3OH} - \langle \chi \rangle|$). *Right*: the PDF and the CDF of the projected angle between the PA of the CH$_3$OH maser distribution and the outflow axes ($|PA_{CH_3OH} - PA_{out}|$). In *both panels* the dashed line is the CDF for random orientation of outflows and magnetic fields, i.e. all angular differences are equally likely. The results of the Kolmogorov-Smirnov test can be found in Table 3.
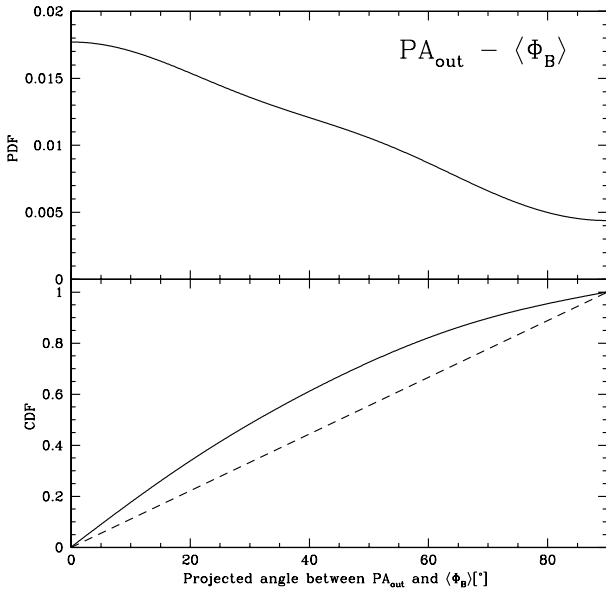
Fig. 8. Probability distribution function (PDF, *top panel*) and cumulative distribution function (CDF, *bottom panel*) of the projected angle between the magnetic field and the outflow axes ($|PA_{out} - \langle \Phi_B \rangle|$). The dashed line is the CDF for random orientation of outflows and magnetic fields, i.e. all angular differences are equally likely. The results of the Kolmogorov-Smirnov test can be found in Table 3

the large-scale molecular outflows. This is supported by a Kolmogorov-Smirnov test that shows a probability of 10% that our distribution of angles is drawn from a random distribution. In the magnetic field total sample, the CH$_3$OH masers are not primarily distributed along the outflows.

Moreover, we empirically found that the linear polarization fraction of unsaturated CH$_3$OH masers is $P_1 < 4.5\%$.

References

Alecian, E., Peralta, R., Oksala, M. E., et al. 2012, Annual meeting of the French Society of Astronomy and Astrophysics, eds. S. Boissier, P. de Laverny, N. Nardetto, et al., 401
Banerjee, R., & Pudritz, R. E. 2007, ApJ, 660, 479
Beltrán, M. T., Girart, J. M., & Estalella, R. 2006, A&A, 457, 865
Beuther, H., Leurini, S., SChilke, P., et al. 2007, A&A, 466, 1065
Bonnell, I. A., Vine, S. G., & Bate, M. R. 2004, MNRAS, 349, 735
Casoli, F., Dupraz, C., Gerin, M., et al. 1986, A&A, 169, 281
Crutcher, R. M. 2005, IAU Symp., 227, 98
Curiel, S., Ho, P. T. P., Patel, N. A., et al. 2006, ApJ, 638, 878
De Buizer, J. M. 2003, MNRAS, 341, 277
Dodson, R., & Moriarty, C. D. 2012, MNRAS, 421, 2395
Donati, J.-F., Howarth, I. D., Bouret, J.-C., et al. 2006, MNRAS, 365, L6
Gibb, A. G., Hoare, M. G., Little, L. T., et al. 2003, MNRAS, 339, 1011
Ginsburg, A. G., Bally, J., Yan, C.-H., et al. 2009, ApJ, 707, 310
Girart, J. M., Beltrán, M. T., Zhang, Q., et al. 2009, Science, 324, 1408
Goddi, C., Moscadelli, L., Sanna, A., et al. 2007, A&A, 461, 1027
Goldreich, P., Keeley, D. A., & Kwan, J. Y. 1973, ApJ, 179, 111
Hennebelle, P., Commerçon, B., Joos, M., et al. 2011, A&A, 528, A72
Heyer, M. H., Carpenter, J. M., & Ladd, E. F. 1996, ApJ, 463, 630
Howard, E. M., Pipher, J. L., & Forrest, W. J. 1997, ApJ, 481, 327
Hunter, T. R., Taylor, G. B., Felli, M., et al. 1994, A&A, 284, 215
Israel, F. P., & Felli, M. 1978, A&A, 354, 1036
Kameya, O., Tatsuhiko, I. H., Hirano, N., et al. 1989, ApJ, 339, 222
Keto, E., & Klaassen, P. 2008, ApJ, 678, L109
Matsumoto, T., & Tomisaka, K. 2004, ApJ, 616, 266
McCutcheon, W. H., Sato, T., Dewdney, P. E., et al. 1991, AJ, 101, 1435

McKee, C. F., & Ostriker, E. C. 2007, ARA&A, 45, 565
McKee, C. F., & Tan, J. C. 2003, ApJ, 585, 850
Minier, V., Booth, R. S., & Conway, J. E. 2000, A&A, 362, 1093
Minier, V., Burton, M. G., Pestalozzi, M., et al. 2005, A&A, 429, 945
Mouschovias, T. C., & Spitzer, L. 1976, ApJ, 210, 326
Oh, C. S., Kobayashi, H., Honma, M., et al. 2010, PASJ, 62, 101
Peters, T., Banerjee, R., Klessen, R. S., et al. 2011, ApJ, 729, 72
Rygl, K. L. J., Brunthaler, A., Reid, M. J., et al. 2010, A&A, 511, A2
Saito, H., Saito, M., Sunada, K., et al. 2007, ApJ, 659, 459
Schilizzi, R. T., Aldrich, W., Andreson, B., et al. 2001, Exp. Astron., 12, 49
Scoville, N. Z., Sargent, A. I., Sanders, D. B., et al. 1986, ApJ, 303, 416
Seifried, D., Banerjee, R., Klessen, R. S., et al. 2011, MNRAS, 417, 1054
Seifried, D., Pudritz, R. E., Banerjee, R., et al. 2012a, MNRAS, 422, 347
Seifried, D., Banerjee, R., Pudritz, R. E., et al. 2012b, MNRAS, 423, L40
Snell, R. L., Huang, Y.-L., Dickman, R. L., et al. 1988, ApJ, 325, 853
Sugitani, K., Fukui, Y., & Ogura, K. 1991, ApJS, 77, 59
Surcis, G., Vlemmings, W. H. T., Dodson, R., et al. 2009, A&A, 506, 757
Surcis, G., Vlemmings, W. H. T., Curiel, S., et al. 2011a, A&A, 527, A48
Surcis, G., Vlemmings, W. H. T., Torres, R. M., et al. 2011b, A&A, 533, A47
Surcis, G., Vlemmings, W. H. T., van Langevelde, H. J., et al. 2012, A&A, 541, A47
Tamura, M., Gatley, I., Joyce, R. R., et al. 1991, ApJ, 378, 611
Vlemmings, W. H. T. 2008, A&A, 484, 773
Vlemmings, W. H. T., Diamond, P. J., van Langevelde, H. J., et al. 2006, A&A, 448, 597
Vlemmings, W. H. T., Surcis, G., Torstensson, K. J. E., et al. 2010, MNRAS, 404, 134
Vlemmings, W. H. T., Torres, R. M., & Dodson, R. 2011, A&A, 529, A95
Wang, Y., Beuther, H., Bik, A., et al. 2011, A&A, 527, A32
Wardle, J. F. C., & Kronberg, P. P. 1974, ApJ, 194, 249
Wilking, B. A., Blackwell, J. H., Mundy, L. G., et al. 1989, ApJ, 345, 257
Wu, Y. W., Xu, Y., Pandian, J. D., et al. 2010, ApJ, 720, 392
Xu, Y., Voronkov, M. A., Pandian, J. D., et al. 2009, A&A, 507, 1117
Zhang, Q., Ho, P. T. P., & Ohashi, N. 1998, ApJ, 494, 636

Appendix A: Tables

In Tables A.1–A.4 we list all the CH_3OH maser features detected towards the four massive star-forming regions observed with the EVN. The Tables are organized as follows. The name of the feature is reported in Col. 1 and the group to which they belong is in Col. 2. The positions, Cols. 3 and 4, are referred to the maser feature used for self-calibration, no absolute positions were measured. The peak flux density (I), the LSR velocity (V_{lsr}), and the FWHM (Δv_L) of the total intensity spectra of the maser features are reported in Cols. 5–7, respectively. I, V_{lsr}, and Δv_L are obtained using a Gaussian fit. The linear polarization fraction (P_l) and the linear polarization angles (χ) are instead reported in Cols. 8 and 9, respectively. The best-fitting results obtained by using a model based on the radiative transfer theory of methanol masers for $\Gamma + \Gamma_\nu = 1 \, s^{-1}$ (Vlemmings et al. 2010; Surcis et al. 2011b) are reported in Cols. 10 (the emerging brightness temperature) and 11 (the intrinsic thermal linewidth). The errors were determined by analyzing the full probability distribution function. The angle between the magnetic field and the maser propagation direction (θ, Col. 14) is determined by using the observed P_l and the fitted emerging brightness temperature. Also for θ the errors were determined by analyzing the full probability distribution function. The circular polarization fraction (P_V) and the Zeeman-splitting (ΔV_Z) are finally in Cols. 12 and 13, respectively. The Zeeman-splitting is determined by fitting the V stoke spectra by using the best-fitting results (ΔV_i and $T_b\Delta\Omega$).

Table A.1. All 6.7-GHz methanol maser features detected in IRAS 06058+2138-NIRS 1.

Maser	Group	RA offset (mas)	Dec offset (mas)	Peak flux density (I) (Jy/beam)	V_{lsr} (km s^{-1})	Δv_L (km s^{-1})	P_l (%)	χ (°)	ΔV_i (km s^{-1})	$T_b\Delta\Omega$ (log K sr)	P_V (%)	ΔV_Z (m/s)	θ (°)
IRAS 06.01	B	−101.002	−242.539	0.11 ± 0.01	1.68	0.22	–	–	–	–	–	–	–
IRAS 06.02	A	−56.857	−34.304	5.95 ± 0.03	11.63	0.32	–	–	–	–	–	–	–
IRAS 06.03	B	−53.453	−252.033	0.18 ± 0.01	3.13	0.22	–	–	–	–	–	–	–
IRAS 06.04	A	−49.836	−29.320	0.11 ± 0.01	8.66	0.16	–	–	–	–	–	–	–
IRAS 06.05	A	−48.453	−15.698	1.09 ± 0.03	10.37	0.23	–	–	–	–	–	–	–
IRAS 06.06	A	−47.815	11.005	0.39 ± 0.01	8.71	0.28	–	–	–	–	–	–	–
IRAS 06.07	A	−46.485	−17.204	5.15 ± 0.14	11.03	0.15	3.2 ± 0.1	23 ± 12	–	–	–	–	–
IRAS 06.08	A	−35.582	−31.330	3.43 ± 0.01	11.87	0.87	–	–	–	–	–	–	–
IRAS 06.09^a	A	−34.359	−11.194	8.75 ± 0.08	11.16	0.18	6.8 ± 0.3	76 ± 6	$0.6^{+0.1}_{-0.1}$	$9.8^{+0.1}_{-0.1}$	–	–	90^{+13}_{-13}
IRAS 06.10	A	−32.284	−26.491	0.41 ± 0.02	11.82	0.33	–	–	–	–	–	–	–
IRAS 06.11	A	−30.104	−11.690	22.21 ± 0.36	10.77	0.52	1.3 ± 0.5	69 ± 10	–	–	–	–	–
IRAS 06.12	A	−23.190	−22.720	2.32 ± 0.03	11.60	0.28	–	–	–	–	–	–	–
IRAS 06.13	A	−20.956	6.157	0.16 ± 0.01	8.40	0.15	–	–	–	–	–	–	–
IRAS 06.14	B	−20.424	−240.074	0.09 ± 0.002	3.13	0.19	–	–	–	–	–	–	–
IRAS 06.15	A	−19.839	−0.356	2.15 ± 0.06	11.21	0.85	–	–	–	–	–	–	–
IRAS 06.16	A	−18.881	−6.853	0.64 ± 0.02	11.69	0.29	–	–	–	–	–	–	–
IRAS 06.17	A	−18.669	41.107	0.72 ± 0.01	8.53	0.19	–	–	–	–	–	–	–
IRAS 06.18	A	−14.733	22.949	0.14 ± 0.01	8.79	0.20	–	–	–	–	–	–	–
IRAS 06.19	A	−12.659	39.961	5.88 ± 0.13	11.12	0.28	–	–	–	–	–	–	–
IRAS 06.20	A	−11.223	80.557	0.25 ± 0.01	7.87	0.25	–	–	–	–	–	–	–
IRAS 06.21	A	−6.489	−1.888	2.51 ± 0.03	11.30	0.28	–	–	–	–	–	–	–
IRAS 06.22^a	A	0	0	93.29 ± 0.16	10.86	0.28	6.0 ± 1.3	76 ± 5	$1.2^{+0.3}_{-0.5}$	$9.6^{+0.6}_{-0.4}$	0.3	3.8 ± 0.6	73^{+17}_{-7}
IRAS 06.23	A	1.117	43.013	10.27 ± 0.29	10.68	0.18	–	–	–	–	–	–	–
IRAS 06.24	A	1.649	4.763	20.64 ± 0.23	10.42	0.36	4.9 ± 0.3	49 ± 2	–	–	–	–	–
IRAS 06.25	A	2.819	2.865	1.17 ± 0.03	11.30	0.27	–	–	–	–	–	–	–
IRAS 06.26	A	6.542	−12.850	10.27 ± 0.30	10.68	0.13	9.2 ± 4.2	−84 ± 4	–	–	–	–	–
IRAS 06.27	A	11.169	−40.705	19.49 ± 0.23	10.72	0.24	2.2 ± 0.8	61 ± 6	–	–	–	–	–
IRAS 06.28	A	15.371	11.868	5.41 ± 0.17	10.99	0.27	–	–	–	–	–	–	–
IRAS 06.29	A	15.743	58.292	0.20 ± 0.01	8.44	0.21	–	–	–	–	–	–	–
IRAS 06.30^a	A	15.797	0.828	50.24 ± 0.23	10.59	0.21	2.3 ± 0.2	67 ± 4	$0.8^{+0.1}_{-0.3}$	$9.9^{+0.4}_{-0.1}$	–	–	64^{+13}_{-38}
IRAS 06.31	A	26.274	43.127	10.68 ± 0.21	10.33	0.15	–	–	–	–	–	–	–
IRAS 06.32	A	32.391	3.937	1.79 ± 0.01	9.98	0.15	–	–	–	–	–	–	–
IRAS 06.33	A	34.093	15.846	3.37 ± 0.12	10.29	0.13	–	–	–	–	–	–	–
IRAS 06.34	A	43.560	3.336	11.18 ± 0.05	9.76	0.22	2.4 ± 0.1	19 ± 8	$1.1^{+0.2}_{-0.3}$	$9.1^{+0.3}_{-0.1}$	–	–	84^{+6}_{-41}
IRAS 06.35	A	45.103	−24.460	7.13 ± 0.22	10.55	0.16	3.3 ± 0.8	69 ± 10	$0.7^{+0.1}_{-0.2}$	$9.3^{+0.3}_{-0.7}$	–	–	84^{+6}_{-16}
IRAS 06.36	A	47.496	−6.975	0.19 ± 0.01	9.41	0.35	–	–	–	–	–	–	–
IRAS 06.37	A	49.996	12.009	13.53 ± 0.33	10.55	0.15	1.9 ± 0.4	59 ± 10	$0.8^{+0.2}_{-0.1}$	$8.9^{+0.3}_{-0.2}$	–	–	76^{+12}_{-37}
IRAS 06.38	A	69.037	11.696	1.65 ± 0.04	9.67	0.22	–	–	–	–	–	–	–
IRAS 06.39	A	76.908	15.019	4.05 ± 0.01	9.76	0.22	–	–	–	–	–	–	–

Notes. $^{(a)}$ Because of the degree of the saturation of these CH_3OH masers $T_b\Delta\Omega$ is underestimated, ΔV_i and θ are overestimated.

Table A.2. All 6.7-GHz methanol maser features detected in IRAS 22272+6358A.

Maser	Group	RA offset (mas)	Dec offset (mas)	Peak flux density (I) (Jy/beam)	$V_{\rm lsr}$ (km s^{-1})	$\Delta v_{\rm L}$ (km s^{-1})	$P_{\rm l}$ (%)	χ (°)	$\Delta V_{\rm i}$ (km s^{-1})	$T_{\rm b}\Delta\Omega$ (log K sr)	$P_{\rm V}$ (%)	$\Delta V_{\rm Z}$ (m/s)	θ (°)
IRAS 22.01		−173.256	265.579	0.062 ± 0.004	−10.51	0.23	–	–	–	–	–	–	–
IRAS 22.02		−138.277	144.333	0.171 ± 0.005	−10.20	0.16	–	–	–	–	–	–	–
IRAS 22.03		−123.872	140.640	0.584 ± 0.005	−10.15	0.23	–	–	–	–	–	–	–
IRAS 22.04		−115.587	130.711	1.378 ± 0.005	−10.20	0.22	–	–	–	–	–	–	–
IRAS 22.05		−101.605	128.204	0.094 ± 0.006	−10.15	0.26	–	–	–	–	–	–	–
IRAS 22.06		−97.550	130.402	0.098 ± 0.008	−10.90	0.17	–	–	–	–	–	–	–
IRAS 22.07		−69.710	157.776	0.354 ± 0.007	−10.86	0.24	–	–	–	–	–	–	–
IRAS 22.08		−69.213	133.293	0.102 ± 0.008	−10.90	0.19	–	–	–	–	–	–	–
IRAS 22.09		−67.695	62.641	0.118 ± 0.005	−9.93	0.14	–	–	–	–	–	–	–
IRAS 22.10		−65.755	179.375	0.081 ± 0.005	−11.16	0.17	–	–	–	–	–	–	–
IRAS 22.11		−65.008	169.689	0.557 ± 0.008	−10.94	0.20	–	–	–	–	–	–	–
IRAS 22.12		−64.784	168.640	0.467 ± 0.008	−10.86	0.21	–	–	–	–	–	–	–
IRAS 22.13		−56.848	155.579	2.720 ± 0.008	−10.90	0.21	0.8 ± 0.2	−75 ± 5	$1.1^{+0.1}_{-0.2}$	$8.5^{+0.4}_{-0.2}$	–	–	77^{+13}_{-38}
IRAS 22.14		−47.295	140.812	1.989 ± 0.008	−10.90	0.23	1.0 ± 0.1	68 ± 17	$1.2^{+0.1}_{-0.2}$	$8.6^{+0.3}_{-0.1}$	–	–	80^{+10}_{-38}
IRAS 22.15		−44.210	129.570	0.310 ± 0.008	−10.72	0.20	–	–	–	–	–	–	–
IRAS 22.16		−36.796	121.681	0.629 ± 0.005	−10.72	0.17	–	–	–	–	–	–	–
IRAS 22.17		−35.900	130.512	1.245 ± 0.007	−11.03	0.14	–	–	–	–	–	–	–
IRAS 22.18		−34.830	143.387	0.221 ± 0.008	−10.94	0.14	–	–	–	–	–	–	–
IRAS 22.19		−29.780	96.726	2.658 ± 0.007	−10.77	0.31	1.7 ± 0.7	−78 ± 4	$1.5^{+0.2}_{-0.2}$	$8.9^{+0.1}_{-1.0}$	–	–	90^{+54}_{-54}
IRAS 22.20		−22.491	87.498	0.321 ± 0.004	−11.30	0.22	–	–	–	–	–	–	–
IRAS 22.21		−13.783	47.733	0.220 ± 0.006	−10.15	0.25	–	–	–	–	–	–	–
IRAS 22.22		0	0	4.838 ± 0.005	−12.83	0.30	–	–	–	–	–	–	–
IRAS 22.23		0.373	−10.288	0.750 ± 0.004	−12.57	0.26	–	–	–	–	–	–	–
IRAS 22.24		1.319	29.022	0.217 ± 0.005	−12.31	0.17	–	–	–	–	–	–	–
IRAS 22.25		47.668	216.942	0.117 ± 0.008	−10.99	1.08	–	–	–	–	–	–	–
IRAS 22.26		215.898	319.664	0.109 ± 0.008	−10.99	0.15	–	–	–	–	–	–	–

Table A.3. All 6.7-GHz methanol maser features detected in S255-IR.

Maser	Group	RA offset (mas)	Dec offset (mas)	Peak flux Density (I) (Jy/beam)	$V_{\rm lsr}$ (km s^{-1})	$\Delta v_{\rm L}$ (km s^{-1})	$P_{\rm l}$ (%)	χ (°)	$\Delta V_{\rm i}$ (km s^{-1})	$T_{\rm b}\Delta\Omega$ (log K sr)	$P_{\rm V}$ (%)	$\Delta V_{\rm Z}$ (m/s)	θ (°)
S255.01	A	−217.801	97.237	0.209 ± 0.009	4.96	0.13	–	–	–	–	–	–	–
S255.02	B	−217.039	−41.428	0.156 ± 0.003	5.70	0.13	–	–	–	–	–	–	–
S255.03	B	−212.685	−62.891	1.212 ± 0.005	5.48	0.13	–	–	–	–	–	–	–
S255.04	B	−212.522	−124.538	3.113 ± 0.015	4.87	0.17	2.2 ± 0.5	39 ± 2	$0.8^{+0.2}_{-0.1}$	$9.0^{+0.3}_{-0.4}$	–	–	80^{+10}_{-21}
S255.05	B	−212.413	−109.398	0.501 ± 0.007	5.00	0.21	–	–	–	–	–	–	–
S255.06	B	−206.100	−53.278	1.707 ± 0.005	5.57	0.17	3.8 ± 0.2	39 ± 4	$0.7^{+0.1}_{-0.1}$	$9.3^{+0.1}_{-0.1}$	–	–	85^{+4}_{-10}
S255.07	B	−205.610	−86.506	0.343 ± 0.004	5.22	0.16	–	–	–	–	–	–	–
S255.08	B	−204.522	−132.717	2.343 ± 0.018	4.74	0.16	1.0 ± 0.3	60 ± 11	$0.8^{+0.1}_{-0.1}$	$8.6^{+0.4}_{-0.4}$	–	–	74^{+14}_{-38}
S255.09	B	−203.923	−19.556	0.399 ± 0.006	5.44	0.14	–	–	–	–	–	–	–
S255.10	B	−201.583	−70.501	0.452 ± 0.005	5.35	0.14	–	–	–	–	–	–	–
S255.11	B	−199.624	−87.763	0.686 ± 0.014	4.78	0.14	–	–	–	–	–	–	–
S255.12	B	−195.977	−140.797	0.297 ± 0.011	4.47	0.15	–	–	–	–	–	–	–
S255.13	B	−195.488	−104.160	0.270 ± 0.004	5.40	0.13	–	–	–	–	–	–	–
S255.14	B	−193.800	−58.836	0.256 ± 0.005	5.40	0.63	–	–	–	–	–	–	–
S255.15	B	−187.760	−151.674	0.198 ± 0.004	4.25	0.84	–	–	–	–	–	–	–
S255.16	B	−172.086	−97.004	0.176 ± 0.006	4.39	1.29	–	–	–	–	–	–	–
S255.17	B	−164.521	−108.042	0.250 ± 0.004	4.08	0.20	–	–	–	–	–	–	–
S255.18	B	−162.126	−156.319	0.394 ± 0.003	4.12	0.22	–	–	–	–	–	–	–
S255.19	B	−160.276	−155.373	0.334 ± 0.003	4.08	0.24	–	–	–	–	–	–	–
S255.20	B	−158.534	−188.637	0.116 ± 0.004	4.17	0.20	–	–	–	–	–	–	–
S255.21	B	−148.194	−146.700	0.668 ± 0.003	4.03	0.22	–	–	–	–	–	–	–
S255.22	B	−144.548	−138.336	0.259 ± 0.004	4.17	0.17	–	–	–	–	–	–	–
S255.23	A	−142.207	231.489	0.268 ± 0.016	4.82	0.15	–	–	–	–	–	–	–
S255.24	C	−135.513	−399.889	0.130 ± 0.003	3.38	0.18	–	–	–	–	–	–	–
S255.25	C	−128.166	−393.681	0.123 ± 0.004	2.23	0.27	–	–	–	–	–	–	–
S255.26	C	−125.989	−373.406	0.361 ± 0.003	3.03	0.23	–	–	–	–	–	–	–
S255.27	C	−125.935	−361.589	0.180 ± 0.003	2.28	0.34	–	–	–	–	–	–	–
S255.28	C	−120.166	−351.229	0.104 ± 0.004	1.31	0.23	–	–	–	–	–	–	–
S255.29	A	−69.172	409.050	0.280 ± 0.016	4.82	0.68	–	–	–	–	–	–	–
S255.30[a]	B	0	0	10.636 ± 0.015	4.61	0.24	4.5 ± 0.3	23 ± 5	$1.1^{+0.1}_{-0.4}$	$9.5^{+0.3}_{-0.1}$	0.3	3.2 ± 0.7	82^{+8}_{-18}
S255.31	B	6.694	5.865	3.689 ± 0.014	4.78	0.20	1.8 ± 0.4	21 ± 7	$0.9^{+0.1}_{-0.2}$	$9.0^{+0.4}_{-0.3}$	–	–	79^{+11}_{-36}

Notes. [a] Because of the degree of the saturation of these CH$_3$OH masers $T_{\rm b}\Delta\Omega$ is underestimated, $\Delta V_{\rm i}$ and θ are overestimated.

Table A.4. All 6.7-GHz methanol maser features detected in S231.

Maser	Group	RA offset (mas)	Dec offset (mas)	Peak flux density (I) (Jy/beam)	V_{lsr} (km s^{-1})	Δv_L (km s^{-1})	P_l (%)	χ (°)	ΔV_i (km s^{-1})	$T_b\Delta\Omega$ (log K sr)	P_V (%)	ΔV_Z (m/s)	θ (°)
S231.01	C	−108.670	51.949	2.287 ± 0.003	−11.82	0.42	0.8 ± 0.4	−7 ± 5	$1.9^{+0.1}_{-0.2}$	$8.5^{+0.9}_{-0.1}$	–	–	90^{+60}_{-60}
S231.02	B	−68.055	47.474	0.177 ± 0.003	−11.51	0.22	–	–	–	–	–	–	–
S231.03	B	−54.975	34.267	0.224 ± 0.003	−11.20	0.22	–	–	–	–	–	–	–
S231.04	B	−53.140	70.908	0.053 ± 0.003	−11.29	0.14	–	–	–	–	–	–	–
S231.05	B	−50.597	−3.765	0.053 ± 0.003	−11.29	0.18	–	–	–	–	–	–	–
S231.06	A_2	−48.914	−104.523	0.062 ± 0.003	−14.27	0.19	–	–	–	–	–	–	–
S231.07	B	−47.498	32.341	0.096 ± 0.003	−11.20	0.15	–	–	–	–	–	–	–
S231.08	B	−46.860	45.284	0.107 ± 0.003	−11.86	0.23	–	–	–	–	–	–	–
S231.09	B	−46.790	33.001	0.073 ± 0.003	−11.33	0.22	–	–	–	–	–	–	–
S231.10	A_2	−45.954	−87.692	0.310 ± 0.004	−14.01	0.29	–	–	–	–	–	–	–
S231.11[a]	A_2	−42.031	−74.463	2.472 ± 0.004	−13.79	0.32	11.3 ± 0.6	−74 ± 2	<0.5	$11.3^{+0.3}_{-0.1}$	–	–	82^{+8}_{-18}
S231.12	A_2	−40.418	−90.500	1.895 ± 0.003	−6.37	0.32	–	–	–	–	–	–	–
S231.13	B	−38.131	21.629	0.065 ± 0.003	−11.20	0.19	–	–	–	–	–	–	–
S231.14	A_2	−32.884	−82.264	0.156 ± 0.003	−7.69	0.36	–	–	–	–	–	–	–
S231.15	B	−27.870	30.174	0.799 ± 0.003	−11.46	0.21	–	–	–	–	–	–	–
S231.16	A_1	−21.973	−36.274	0.257 ± 0.003	−15.02	0.39	–	–	–	–	–	–	–
S231.17	A_1	−19.071	−30.800	0.620 ± 0.003	−14.23	0.33	–	–	–	–	–	–	–
S231.18	A_1	−16.947	−23.762	0.143 ± 0.003	−14.54	0.27	–	–	–	–	–	–	–
S231.19	A_1	−9.147	11.021	0.174 ± 0.006	−13.18	0.42	–	–	–	–	–	–	–
S231.20[a]	A_1	−7.882	−11.410	3.900 ± 0.004	−14.14	0.34	5.8 ± 1.1	47 ± 1	$1.2^{+0.3}_{-0.5}$	$9.6^{+0.5}_{-0.7}$	–	–	83^{+7}_{-16}
S231.21	A_1	−3.471	−13.863	0.261 ± 0.008	−13.13	0.33	–	–	–	–	–	–	–
S231.22	A_1	−2.403	−4.982	0.539 ± 0.004	−13.66	0.39	–	–	–	–	–	–	–
S231.23	A_1	0	0	23.419 ± 0.010	−12.96	0.34	4.0 ± 0.4	48 ± 1	$1.7^{+0.4}_{-0.5}$	$9.3^{+0.4}_{-0.2}$	–	–	80^{+8}_{-41}
S231.24	A_1	5.467	9.663	0.612 ± 0.005	−13.31	0.38	–	–	–	–	–	–	–
S231.25[a]	A_1	5.815	4.520	6.634 ± 0.011	−12.87	0.30	5.3 ± 0.6	48 ± 1	$1.3^{+0.2}_{-0.5}$	$9.6^{+0.4}_{-0.1}$	–	–	82^{+8}_{-18}
S231.26	D	14.231	−108.620	0.105 ± 0.003	−12.17	0.22	–	–	–	–	–	–	–
S231.27	A_1	15.206	18.288	0.389 ± 0.005	−13.22	0.34	–	–	–	–	–	–	–
S231.28	A_1	17.330	21.011	0.153 ± 0.004	−13.35	0.40	–	–	–	–	–	–	–
S231.29	D	22.588	−116.097	0.294 ± 0.003	−12.08	0.25	–	–	–	–	–	–	–
S231.30	D	25.038	−109.062	0.302 ± 0.010	−12.96	0.15	–	–	–	–	–	–	–
S231.31	D	28.148	−117.458	0.188 ± 0.006	−13.18	0.90	–	–	–	–	–	–	–
S231.32	D	28.949	−67.051	0.103 ± 0.003	−12.39	0.18	–	–	–	–	–	–	–

Notes. [a] Because of the degree of the saturation of these CH_3OH masers $T_b\Delta\Omega$ is underestimated, ΔV_i and θ are overestimated.